Rock Mechanics and Rock Engineering (2020) 53:5489–5510
https://doi.org/10.1007/s00603-020-02222-z

ORIGINAL PAPER

Continuous Compaction and Permeability Evolution in Longwall Gob Materials

Ang Liu[1] · Shimin Liu[1] · Gang Wang[2] · Derek Elsworth[1]

Received: 16 March 2020 / Accepted: 5 August 2020 / Published online: 18 August 2020

Abstract
Understanding the evolution of gob compaction and related gas transport behavior is necessary for the planning and optimization of gas ventilation and control in longwall coal mines. In particular, the detachment of the undermined roof into the gob leaves a loosely compacted perimeter that skirts the longwall panel. This permeable gob perimeter in plan view forms as a result of shear separation from support provided by the solid ribs. This detachment and the resulting rotated and reduced stresses limit compaction, elevate permeability and exert significant control on gas flow during active longwall mining operations. We report gob compaction experiments on in-mine-collected fragmented rock and conduct mechanical compaction on stacked samples that are either uniformly coarsening upwards (case A) or are coarsening upwards, but capped by a segregated upper layer of coarse rock (case B). Observed compaction is linked to a capillary model representing porosity reduction and permeability evolution. As applied uniaxial stress increases from 0 to up to ~ 2000 kPa, the porosity decreases from 0.64 to 0.41(~ 36%) for the uniform stacked material (A) and but only from 0.66 to 0.51 (~ 23%) where the gob is topped with a layer of coarse "roof" rock simulants (B). Particle–particle self-adjustment dominates the compactive behavior at initial low stress and results in significant strain—followed by a linearly elastic region through the remainder of loading. The elastic regime is used to predict the permeability of the loosely compacted gob, considering the redistribution of stresses induced by shear collapse at the rib. Permeability evolution is scaled through the evolving compactive strains and particle size distribution of the fragmented rock, enabling results to be up-scaled to mine scale. These results provide a first rational method for analyzing the interactions between caved gob and the ventilation system towards mitigating gas concentrations and minimizing the hazard.

Keywords Gob materials · Uniaxial stress loading · Fractal dimension · Gob permeability · Friction force

1 Introduction

Longwall mining is an efficient and economically favorable method for the recovery of coal (Peng 2008; Alehossein and Poulsen 2010; Sajjad et al. 2019; Wang et al. 2020). In a typical longwall mining system, the longwall panel advances incrementally as the coal is continuously extracted (Fan and Liu 2017; Wang et al. 2019). Ideally, the unsupported immediate roof and the overlying strata will fracture and collapse to form the gob—avoiding excessive cantilevered loading by the intact roof to the face supports. This caved zone will compact as the face advances and arching support diminishes. This jumble of irregular caved blocks of rock and residual coal fill the caved zone and form the dynamic gob region. Depending on the degree of compaction of the caved gob materials, the height of the caved zone may reach ~ 4-to-11 times the thickness of the coal seam (Karacan 2009a, b; Li et al. 2020). Within the mine gob region, the compacted rock/coal mass provides viable, complex and dynamic pathways for airflow and the concurrent migration of methane (Karacan 2010). Although the gas flow pathways may constrict with compaction, the high permeability pathways will endure and will affect the leakage of ventilation airflow from working face to the gob, the flow of methane

✉ Shimin Liu
szl3@psu.edu

[1] Department of Energy and Mineral Engineering, G3 Center and Energy Institute, The Pennsylvania State University, University Park, PA 16802, USA

[2] Mine Disaster Prevention and Control-Ministry of State Key Laboratory Breeding Base, Shandong University of Science and Technology, Qingdao 266590, People's Republic of China

from surrounding sources towards the gob and into the mine face, and the performance of methane extraction gob gas ventholes (Karacan 2009a, b; Karacan et al. 2007). Thus, understanding and predicting the compaction behavior of the caved zone can provide a mechanism-based approach to define the evolution of gas flow behavior and in proposing effective gas mitigation strategies. The goal of this is to minimize gas outing and its related mine safety hazard.

The overburden stress in the caved zone evolves dynamically as a result of repetitive loading then unloading (Zhang and Zhang 2019; Zhao et al. 2019). This quasi-static loading modulates porosity and permeability as a function of both stress-induced deformation and stress-induced damage (Wang et al. 2018; Zhu et al. 2016). By recalling the Mohr–Coulomb failure criterion—even the criterion does not govern the compaction of broken rocks in the gob, where evolving tensile or shear stresses exceed the truncated Mohr–Coulomb failure criterion, the broken rock blocks comprising the gob will fail and compact towards a final equilibrium state. Thus, the overburden stress profile and its evolution uniquely determine the deformation in the caved zone, which will also influence the dimensions and shapes of the broken rock together with the associated evolution of porosity and permeability.

The gob compaction process can be idealized as one-dimensional quasi-static consolidation (Karacan 2010). Figure 1 shows a schematic representation of longwall mining with a shearer as well as the distribution of rock/coal mass in the caved gob. Field observations (Forster and Enever 1992; Adhikary and Guo 2014; Zhang et al. 2016) suggest a gas drainage model illustrated in Fig. 1b. Indeed, the caved rock mass comprising the gob is heterogeneous but structured as a permeable boundary gob perimeter-shaped ring skirting the more fully compacted gob to the interior (Fig. 1c). This structure results from the action of the rib supports significantly influences the stress and permeability distribution (Fig. 1c) through this loosely compacted zone B. Vertical compaction within this zone mobilizes friction from the local rib confinement along the boundary between the rock mass and the rib. This frictional force rotates the principal stresses within the loosely compacted Zone B. Thus, the compactive behavior within this skirting "gob perimeter" shaped ring will be linked to the local rib confinement (Fig. 1b, c), concomitantly impacting the porosity and permeability evolution.

We present experimental observations of scaled-gob compaction and dynamic permeability evolution using mine roof-rock materials. We develop an analytical model to evaluate the re-distribution of stresses within the loosely compacted Zone B adjacent to the rib. This defines the impact of the local shear stress on the volumetric response of the gob rock mass and its impact on permeability. The analytical

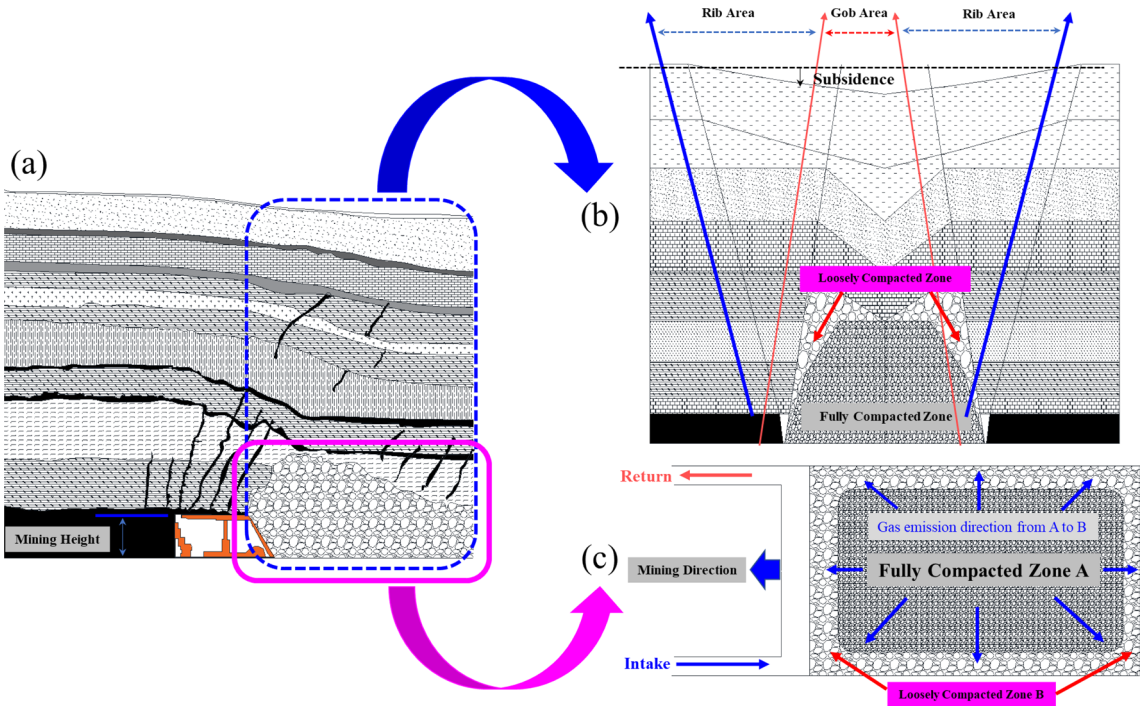

Fig. 1 Schematic of longwall mining and the distribution of rock/coal mass in the gob region: **a** schematic representation of longwall mining with a shearer [modified from Karacan (2009a)]. **b** Gas-flow model proposed for the gob area and rib area [modified from Forster and Enever (1992)]. (c) Plane-view of the interior compacted gob zone skirted by a lightly-compacted O-shaped ring

models are validated against available observations with probability density functions of the particle size distribution providing the link between laboratory and field scale behavior. The validated models are then used as mechanism-based model to predict porosity/permeability evolutions in the gob region.

2 Background and Previous Studies

As the longwall mining panel progressively advances, the gob rock mass, including the immediate roof rock, overlying strata, and residual coal gradually compacts. The resulting compactive state is highly related to the dimensions, gradation, shapes, and distribution of the broken rock blocks (Arya and Paris 1981; Auset and Keller 2004; Mortensen et al. 2005; Sirivithayapakorn and Keller 2003; Wu et al. 2008). Specifically, the gob material is highly fragmented with irregular shapes of various sizes. The rock fragment size distribution influences the mechanics of fluid transport in the fragmented medium (Karacan 2010). The size distribution of the fragmented rock blocks is one key property that links laboratory scale response to field scale—mobilizing the power of digital imaging (Rieu and Sposito 1991). Mechanical deformation may be digital imaged to establish a three-dimensional (3D) model then allowing the simulation of stress–seepage coupling effects (Zhao et al. 2018). The disordered nature of the broken rock blocks is amenable to fractal description for the fragment size distributions enabling fractal porosity and permeability models to be developed. Specifically, the permeability and porosity expressions can be shown as Karacan (2010):

$$k = \frac{\pi}{16A_T}\frac{L_0^{(1-D_T)}}{\alpha}\frac{D_P}{2.531 + D_T - D_P} \times r_{max}^{2.531+D_T}\left[1 - \left(\frac{r_{min}}{r_{max}}\right)^{2.531+D_T-D_P}\right], \quad (1)$$

where k is the permeability, m^2; A_T is the total area to flow, m^2; L_0 is the representative length, m; α is the shape factor in the Hagen–Poiseuille equation, dimensionless; D_T is the tortuosity fractal dimension, fractal dimension; D_P is the pore-area fractal dimension, fractal dimension; r_{min} and r_{max} are the minimum and maximum pore sizes respectively, m, and:

$$\phi_{i+1} - \phi_i = -\Lambda\left[\frac{\sigma_{i+1}^{\frac{m(D_F-1)}{2}-1}}{\frac{m(D_F-1)}{2}-1} - \frac{\sigma_i^{\frac{m(D_F-1)}{2}-1}}{\frac{m(D_F-1)}{2}-1}\right], \quad (2)$$

where ϕ_{i+1} and ϕ_i are successive porosities under compaction, dimensionless; Λ is plastic compressibility index, 1/MPa; D_F is the fragmentation fractal dimension, fractal dimension; m is the Weibull modulus, dimensionless; σ_{i+1} and σ_i are the applied macroscopic stresses, MPa.

The above fractal theory-based models are essential in understanding the effects of particle size/spatial distribution on the evolution of porosity and permeability. Incorporating the evolution of average stress enables dynamic compaction effects to be explicitly incorporated into the permeability model. In addition to porosity and permeability models accommodating fractal theory, the Carman–Kozeny equation may be applied to estimate gob permeability as Esterhuizen and Karacan (2007):

$$\frac{k}{k_0} = 0.241\left[\frac{\phi^3}{(1-\phi)^2}\right], \quad (3)$$

where k_0 is the initial permeability of the broken rock at the maximum porosity, m^2; and ϕ is the porosity, dimensionless. One concern related to Eq. (3) is the determination of the initial permeability, which is challenging due to the inaccessibility of the gob environment.

Gob permeability is highly dependent on the in situ overburden stresses (Lowndes et al. 2002). Semi-empirical formulae quantify fractured rock permeability, defining an exponential relationship between permeability and the volumetric strain as Jozefowicz (1997):

$$k = -4\times10^{-16}\varepsilon_v^3 - 6\times10^{-15}\varepsilon_v^2 - 7\times10^{-14}\varepsilon_v + 10^{-11}, \quad (4)$$

where ε_z is the volumetric strain, dimensionless. In addition, exponential relations link fracture permeability to stress as Karacan et al. (2007):

$$k_v = k_{v0}\exp\left[-0.25\left(\sigma_{zz} - \sigma_{zz0}\right)\right], \quad (5)$$

$$k_h = k_{h0}\exp\left[-0.25\left(\sigma_{xx} - \sigma_{xx0}\right)\right], \quad (6)$$

where k_v and k_h are the independent permeabilities in the vertical and horizontal directions, m^2; k_{v0} and k_{h0} are the initial permeabilities, m^2; σ_{zz} and σ_{xx} are the prevailing stresses and σ_{zz0} and σ_{xx0} are the initial vertical and horizontal stresses, respectively, MPa.

Such models of porosity and permeability are stress dependent. Stress-induced rock mass deformation and damage can significantly impact porosity and permeability ass. Specifically, the stress-dependent permeability can be linked to porosity evolution (Eqs. (1) and (3)) or directly developed from the impact of stress level on volumetric strain (Eqs. (4–6)). These models implicitly show that the stress level, as well as the stress-dependent rock mass properties, drives the dynamic changes in porosity/permeability. Significant effort has been devoted to characterizing the stress–strain relationship for gob rock masses. The classical quantitative stress–strain relationship for compacting gob can be defined as

$$\sigma_v = \frac{E\varepsilon_v}{1-\varepsilon_v/\varepsilon_m}, \tag{7}$$

where σ_v is the vertical stress, MPa; E is the initial tangent modulus of the broken rock, MPa; ε_v is the vertical strain, dimensionless; ε_m is the limiting maximum vertical strain, dimensionless. Among these parameters, E and ε_m can be quantified as Zhang et al. (2019):

$$E = \frac{10.39\sigma_c^{1.042}}{b^{7.7}}, b = 1 + \frac{c_1 h + c_2}{100}, \varepsilon_m = \frac{b-1}{b}, \tag{8}$$

where b is the bulking coefficient, dimensionless; σ_v is the maximum uniaxial compressive strength, MPa; c_1 and c_2 are the coefficients related to the strength of the immediate roof, which can be fitted from the experimental data based on the semi-empirically equation; h is the height of the caved zone, m. Based on the assumption of elastic response, a conceptual model for the stress–strain constitutive law may be developed by assuming that the contact connection between two adjacent rock particles is similar to that in a cubic mass (Fan and Liu 2017):

$$\sigma_v = \frac{E_b}{\alpha}\varepsilon_v, \tag{9}$$

where E_b is the elastic modulus of rock particles, MPa; α is the uniaxial elastic modulus coefficient, dimensionless, which is an empirical parameter based on a conceptual model and can be fitted through experimental data. In addition to the evolving stress level in the caved zone, the stress-dependent material properties are also sensitive to the stress level. Based on deformation experiments, the stress-dependent secant modulus exhibits a linear relationship with the stress level as Pappas and Mark (1993):

$$E = a\sigma_v + b, \tag{10}$$

where E is the secant modulus of the rock particles, MPa; a and b are the experimental fitting parameters, dimensionless. Also, the elastic modulus and Poisson ratio of the caved rock mass evolve with the one-dimensional consolidation (Zhang et al. 2019). Typically, the bulk modulus of the broken rock blocks evolves with the accumulation of vertical strain and the maximum vertical strain as

$$K = \frac{4G}{3} = \frac{E_0}{2\left(1-\varepsilon_v/\varepsilon_m\right)}, \tag{11}$$

where G is the shear modulus, MPa; and E_0 is the initial tangent modulus of the broken rock blocks.

Previous studies mainly concentrated on empirical and regression-fit experimental observations. Some analytical models attempted to link stress-induced deformation and damage with the evolution of porosity and permeability (Guo et al. 2015, 2009). Accommodating stress-dependent rock mass properties improved predictions of volumetric response and gas flow behavior in the caved zone. However, the majority of these studies assume that the overburden stress is the only compactive force impacting porosity and permeability evolution, neglecting the important role of rib confinement, as illustrated in Fig. 1c.

In this study, we report the physical gob compaction experiments on in-mine-collected fragmented rock and conduct mechanical compaction on stacked samples that are uniformly coarsening upwards. Based on the experimental results, the specific emphasis is made on the variation in compactions between the outer and central regions as this is considered analogous of the gob abutments. The detachment of the undermined roof into the gob leaves a loosely compacted perimeter that skirts the longwall panel. This permeable perimeter forms as a result of shear separation from support provided by the solid ribs. The theoretical models for quantifying the rotated stresses and the porosity/permeability were proposed based on the conceptual model origins from the experimental observations in this study and idealized geometry models from literatures (Forster and Enever 1992; Karacan 2009a). Since we cannot collect enough effective data under very high loadings based on our own experimental setup, the proposed models were subsequently validated against with the public data (Pappas and Mark 1993). The validated models were then used as mechanism-based models to predict the permeability evolutions. The predicted results were analyzed and discussed by comparing with other work from literature (Karacan 2010). This study can ultimately provide a comprehensive model framework to study the porosity/permeability evolution under in situ complex inaccessible condition, which can be used for the ground control and operation optimizations for gob degasification strategies.

3 Experiments and Observations

3.1 In-mine Sample Collection and Experimental Design

Caved broken rock was collected from a deep longwall mining operation in China at the Tangkou coal mine. The Tangkou coal mine is located in Jining city, Shandong Province, China. The actively mined seams are of Permian (Shanxi formation) and Carboniferous (Taiyuan formation) (Fig. 2a) ages. These comprise six coal seams numbered as #3, #6, #10, #15, #16, and #17 (Fig. 2a) with the #3, #16, and #17 as the primary targeted seams for longwall mining. Annual production is planned at ~ 5 million tons/year (Liu et al. 2020b). The #3 coal seam is mined by the LTTC mining method and is the object of this study. A field in-mine ventilation survey

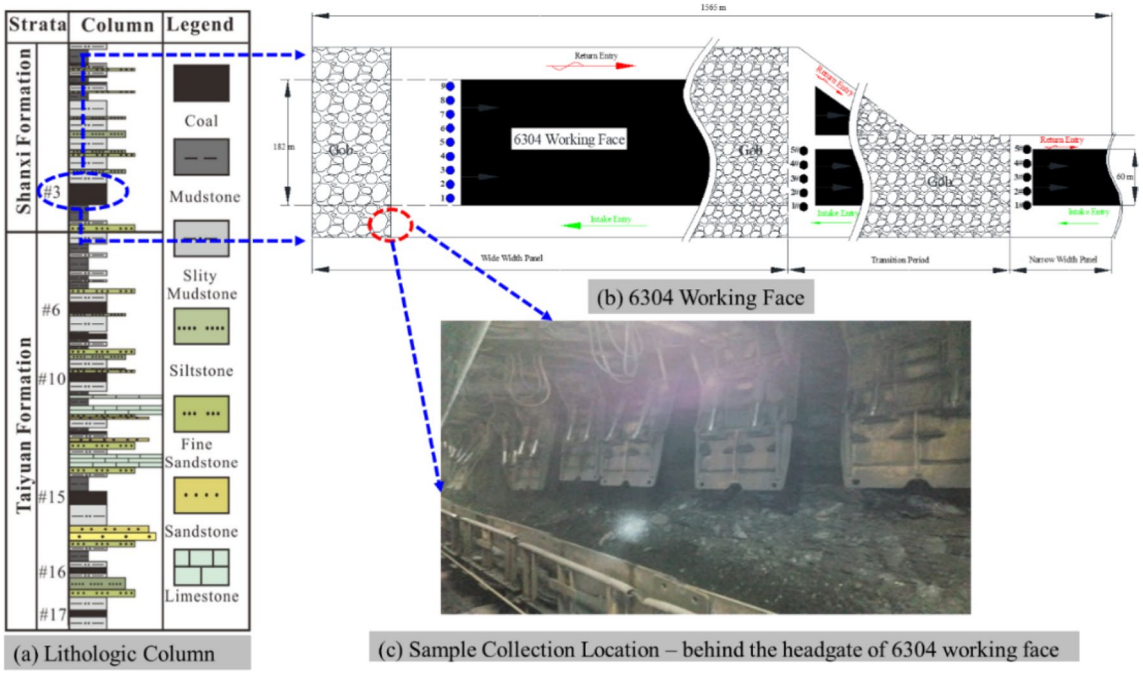

Fig. 2 Schematic of the 6304 working face and sampling location: **a** lithologic column. **b** 6304 working face. **c** Sample collection location behind the shields

was conducted at the 6304 working face within the #3 coal seam, subject to the panel layout illustrated in Fig. 2b. The average thickness of the coal seam at the 6304 working face is ~ 9.76 m, with a detailed mine layout reported previously (Liu et al. 2020b). An initial width of 182 m transitions to a final narrow panel width of 60 m with a working face length of ~ 1565 m (Fig. 2b).

Compaction experiments used caved rock from multiple locations immediately behind the shield following caving, as shown in Fig. 2c. The density of the collected mudstone sample was measured as ~ 2.1 g/cm^3. The collected caved rock blocks were manually selected with diameters less than 25 cm. The broken rock samples were classified into fractions with edge dimensions ≤ 5 cm, 5–10 cm, 10–15 cm, and ≥ 15 cm (Fig. 3). These gob materials were used in compaction tests in the laboratory.

The experiments simultaneously measure both displacement and flow in the simulated gob samples. The experimental system (Fig. 4) comprises a high-stress uniaxial (zero lateral strain) rock compaction chamber to contain the caved rock mass (Fig. 4a). The cylindrical chamber is 40 cm in diameter and 60 cm in height, as shown in Fig. 4a. The chamber was placed in a loading frame with a maximum loading capacity is 600 kN with both axial load and vertical displacement continuously monitored.

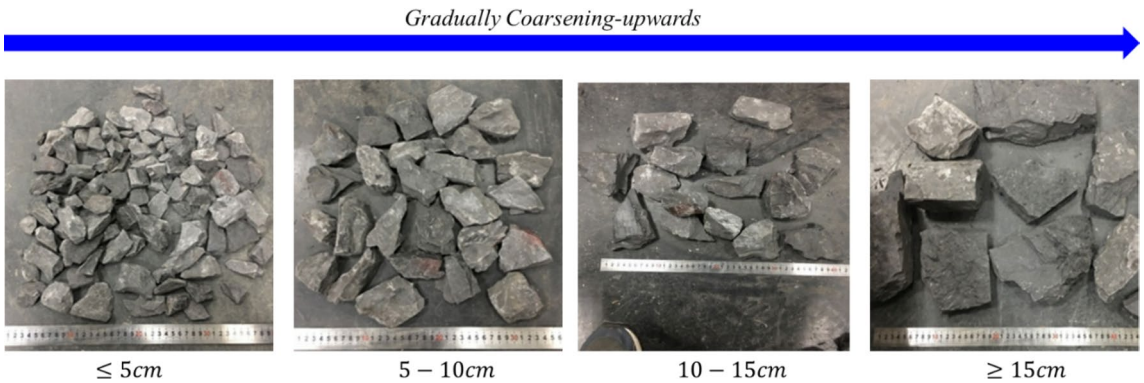

Fig. 3 Gob materials collected from longwall coal mine

Fig. 4 Schematic of the experimental setup. **a** Schematic of the load deformation and fluid flow testing system. **b** Inside view of the sample chamber. **c** Gas outlet and pressure transducer. **d** Exterior view of the sample chamber. **e** Mass flowmeter

Field observation (Fig. 2) identifies distinct layering in the caved rock mass—with component rock block sizes increasing in size from floor to roof. To replicate this observed structure, the fragmented samples were weighted and mixed in different modes for both two tests, as shown in Fig. 5.

Then, experiments were conducted in two modes (Table 1 and Fig. 6): Test A with layers gradually coarsening-upwards and Test B with similar coarsening-upwards layers capped with single coarse top layer. In Test A, the rock samples (dimensions of ≤ 5 cm and 5–10 cm) were packed in the first layer with the mass ratio of 1:4. That is, 20% by weight

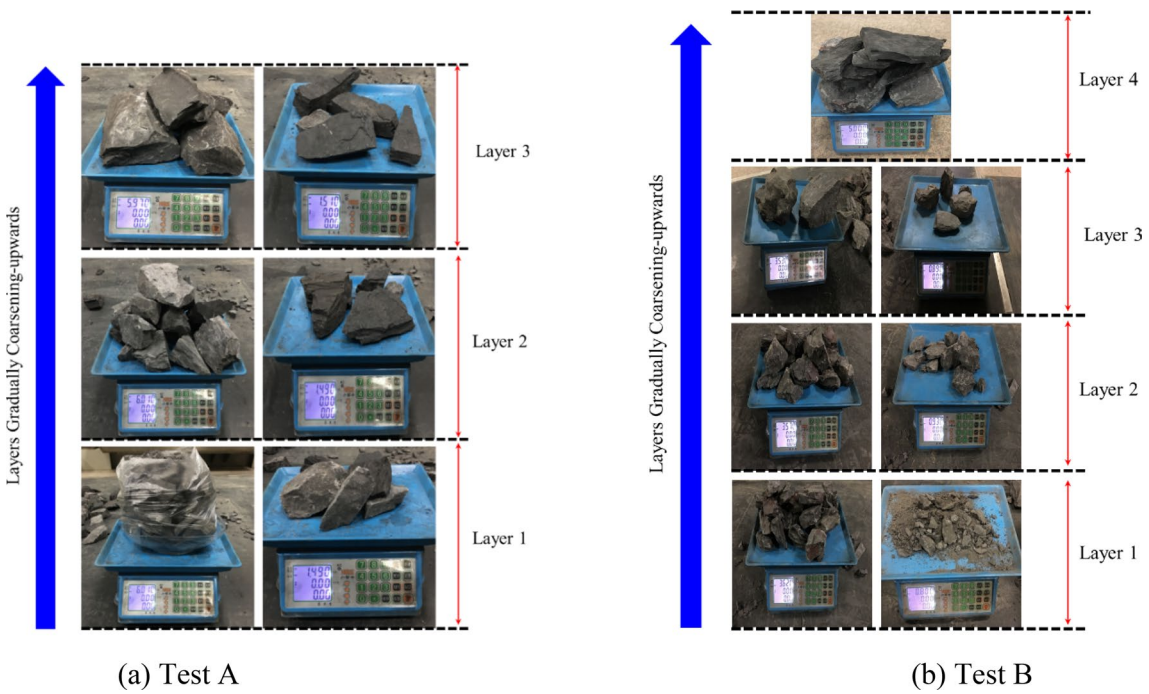

Fig. 5 Different layering behavior of gob materials in Tests A and B

Table 1 Raw data for the two tests

Tests	Height(cm)	Weight (kg)	Particle size distribution (mass percentage)				Porosity	
			≤ 5 cm	5–10 cm	10–15 cm	≥ 15 cm	Initial	Final
Test A								
Layer 1	8	7.50	20%	80%	–	–	0.64	0.43
Layer 2	8	7.50	–	20%	80%	–		
Layer 3	8	7.48	–	–	20%	80%		
Test B								
Layer 1	5	4.42	20%	80%	–	–	0.66	0.51
Layer 2	5	4.50	–	20%	80%	–		
Layer 3	5	4.42	–	–	20%	80%		
Layer 4	5	5.00	–	–	–	100%		

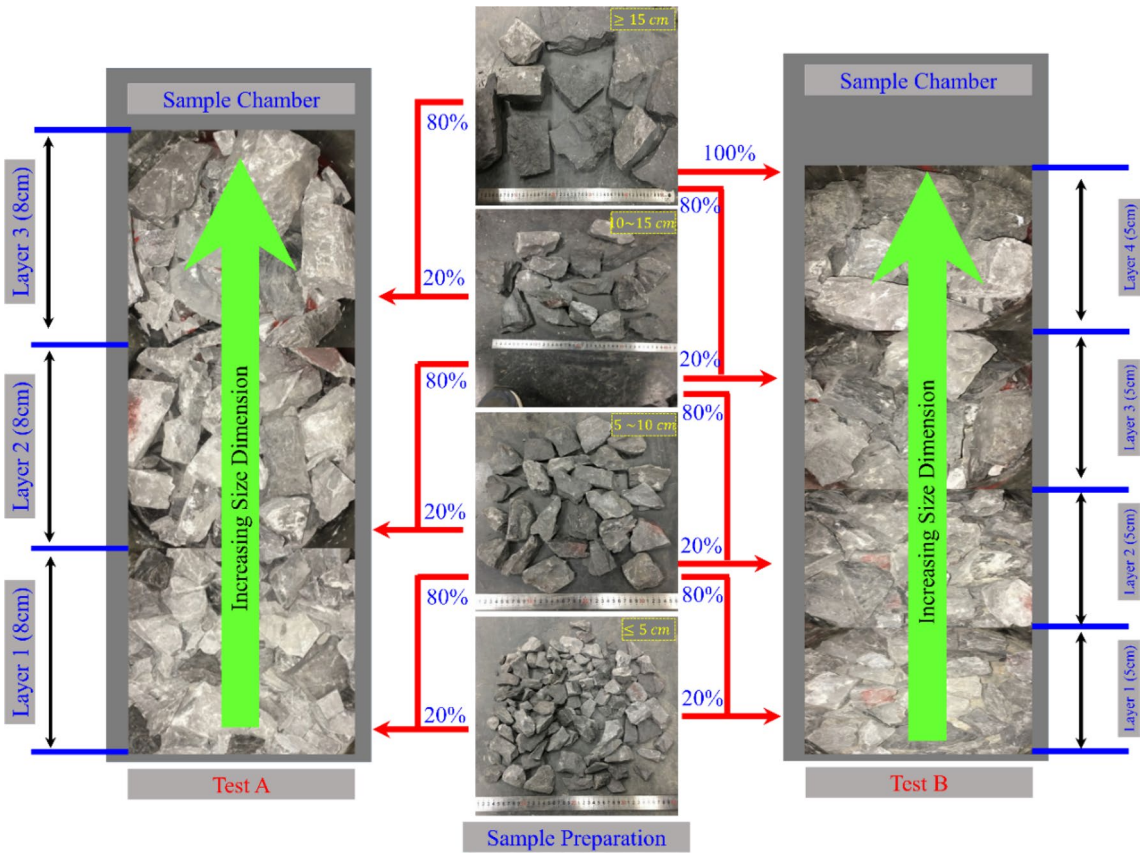

Fig. 6 Schematic of experimental design for Tests A and B

of ≤ 5 cm and 80% by weight of 5–10 cm, packed as the first layer as shown to the bottom left of Fig. 6. For the second layer, the mass ratio remains as the same at 1:4 but with incremented gradations of 5–10 cm and 10–15 cm, respectively. The third layer is finally packed with further incremented gradation dimensions of 10–15 cm and 15–25 cm again at a 1:4 mass ratio. All three layers in Test A have the same packing height of approximately 8 cm and the same rock mass weight of ~ 7.5 kg, as shown in Fig. 6. Similarity, the new four layers of the second test B were packed as shown in Fig. 6. The four layers in Test B again have a uniform packing height now of approximately 5 cm and the same rock mass weight of ~ 4.5 kg in each layer—but the uppermost capping layer comprises the coarsest fraction, only—representing the in situ observation of a coarse-graded top-gob. For Tests A and B, the loading rates were set as 0.1 kN/s and 0.05 kN/s, respectively, with the maximum applied loads for the two tests as 300 kN and 200 kN, respectively. It should be noted that the two packing types are the reasoning results of the field observation and other

work from literature (Zhao et al. 2018), which replicate different layering behavior of gob materials. The aim of two different experimental loading rates in Test A and Test B was to achieve two totally different scenarios. If we can observe the similar permeable gob perimeters from two totally different tests, then it is confident to build the conceptual model. Future studies might incorporate detail layering information and loading rate with respect to lithology and overburden stress respectively.

3.2 Mechanical Behavior of the Broken Rock Mass with Uniaxial Loading

Figure 7 shows images of the fragmented rock mass both before then after the compaction experiments for the contrasting gradations of Tests A and B. Apparent is that the rock blocks in all layers compact, crush and fail into smaller sized fragments. In both Tests A and B, the fragments in the center of the sample were fully compacted with those on the periphery relatively loosely compacted and less damaged—a direct miniature analog of behavior at gob scale—although this is not the focus of the experiments. For both Tests A and B, the lower layer (i.e. basal layer) was severely compacted and crushed compared to the upper layers (i.e. layer 3 in test A or layer 4 in test B). As shown in Figs. 6 and 7, the fragments in both tests were packed with layers gradually coarsening from bottom to top. Based on the results from Karacan (2010) and Fan and Liu (2017) and our experimental results, it can be justified that the relatively large fragmented rock mass at the top layer tends to have flat surface (i.e. cuboid,

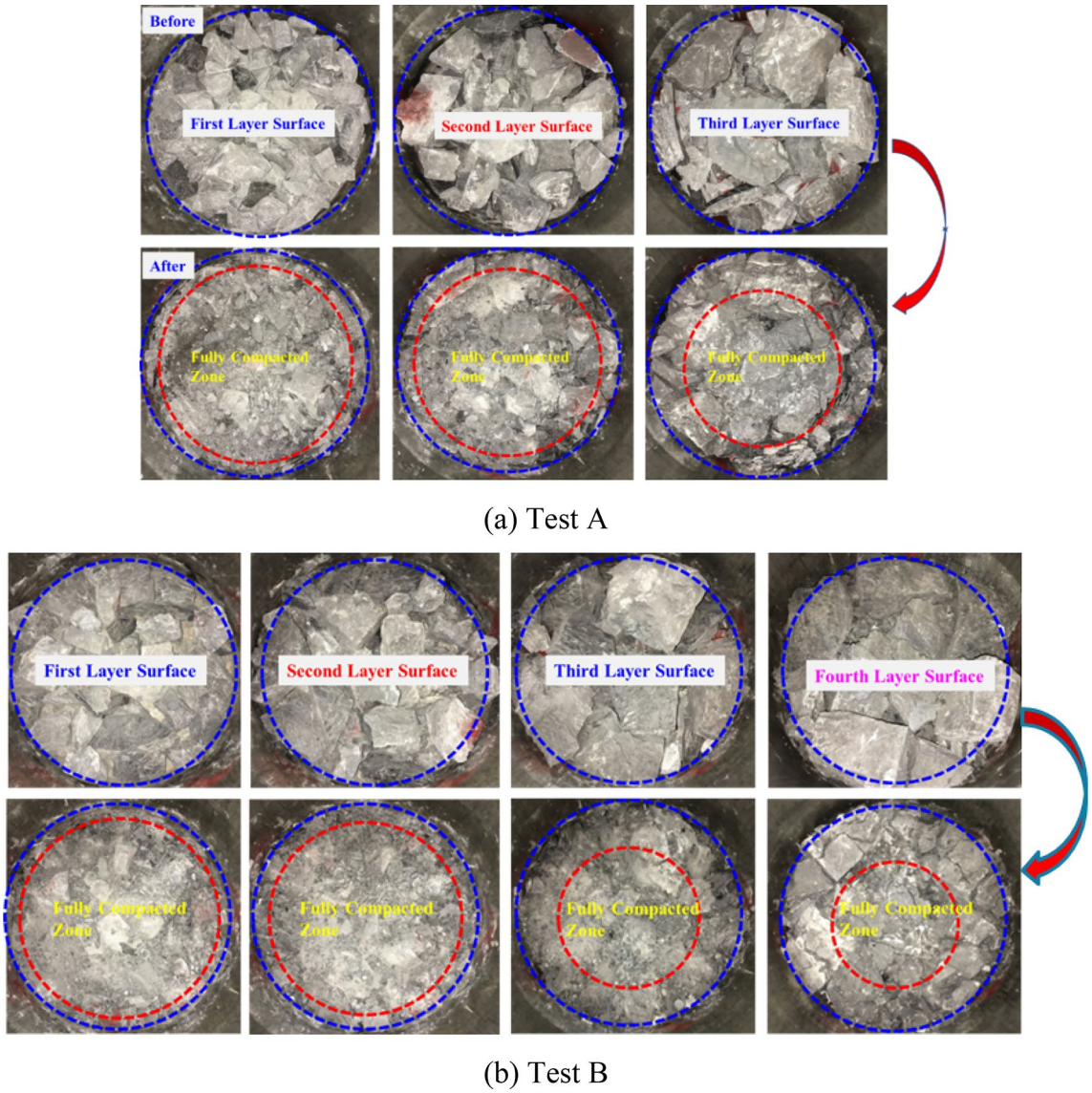

Fig. 7 Mine-roof rock mass both before (top) and after (bottom) compaction experiments of Tests A and B

polyhedron) and the mutual contact between large fragments can be regarded as areal contact. The smaller sized fragments in bottom layer tend to have sharp and uneven surfaces, i.e. triangular awl shape. The irregular distribution of smaller sized fragments in bottom layer tends to lead to prevailing point contacts across fragments. The cumulative and statistical contact area in top layer is expected to be higher than bottom layer. With the same applied vertical force, the smaller sized fragments at the bottom are subject to higher point-contact loads than the upper layers. The experimental results indirectly represent the "O-shaped" type compaction behavior for the gob at lab scale, analogous to Fig. 1c as a result of rib support and friction induced forces.

Figure 8a shows the mechanical response of the fragmented rock under uniaxial loading. The stress–strain curves show distinct differences between the gradations of Tests A and B. The response may be separated into two segments—initial high-compaction followed by elastic compaction (Fig. 8a). During initial compaction, the stress–strain response remains flat with the initial small applied seating stress. After the initial compaction, the response switches to linearly elastic. For the continuously coarsening upwards gradation of Test A, a strain of ~ 0.25 is the threshold to elastic response at an average stress of ~ 0.38 MPa (corresponding to a force of 48.33 kN). The average stress is computed from the force applied over the average cross-sectional area of the experimental chamber. The maximum strain for Test A is ~ 0.39 corresponding to a maximum stress of ~ 1.95 MPa (corresponding to a force of 245.26 kN) during the second load cycle. For Test B, ~ 0.17 is the threshold strain for elastic response representing an average stress of 0.41 MPa (corresponding to a force of 51.38 kN). The maximum strain is ~ 0.30 at a stress of ~ 1.59 MPa (corresponding to a force of 200 kN). Although similar two-stage trends are observed for both Tests A and B, comprising the same materials, the differing thresholds result from the different stacking and packing configurations—both are coarsening upwards but Test B has a larger gradation and is capped with a single course layer, or different loading rates. This indirectly suggests that the overburden strata control gob compaction as illustrated in Fig. 1b. Based on the experimental data, we infer that the gob material can be treated as a linear and elastic medium after an initial seating-in compaction. However, the elastic assumption may not be appropriate for the initial compaction period with excessive deformation under low stress conditions. Additionally, we need to point out that the elastic behavior of the compacted gob materials cannot be applied for unloading process. Strictly, the compacted gob materials are not continuous mediums, which consist of many fragments with different sizes. As the loadings continuously increase, the contacts between fragments will become more and more tight and the linear elastic behavior will be much more obvious. Conversely, any unloading of the gob materials will easily break the contacts between the compacted fragments and thus the linear elastic assumption is untenable for unloading process.

For both Tests A and B, the porosity of the fragmented rock mass in the sample chamber was calculated from $\phi = \frac{V_r}{V_c}$, where V_r is the total volume of the broken rock blocks—total volume of the sample is assumed constant as $V_r = \frac{m}{\rho}$ (where m is the total mass of the sample, ρ is the density of the rock sample). V_c is the time-dependent volume of the sample chamber in use, which includes the constant sample volume and the stress-dependent void volume. The time-dependent volume V_c is calculated from

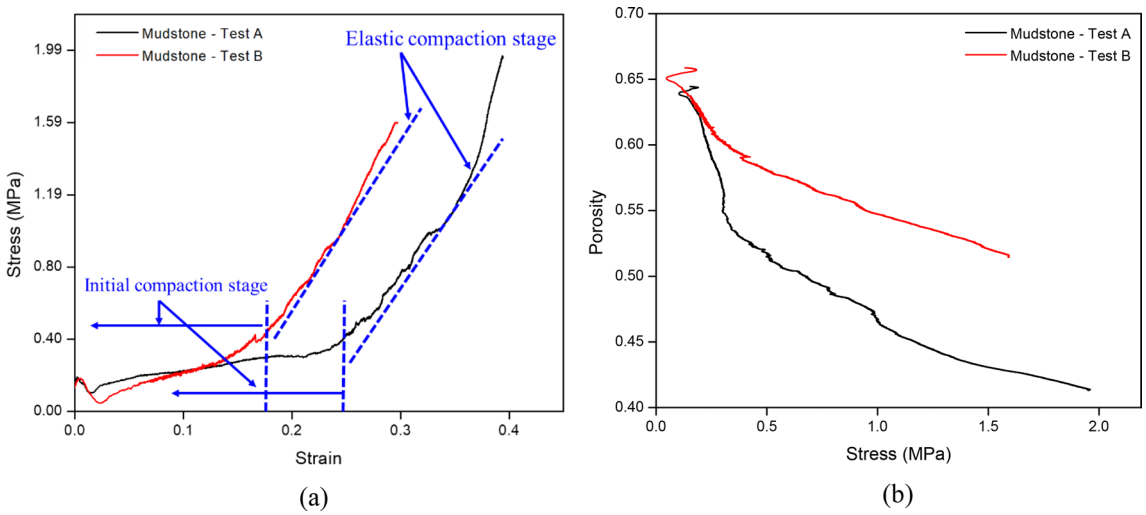

Fig. 8 Mechanical behavior and porosity evolution of the broken roof-rock masses under uniaxial loading. **a** Stress–strain response. **b** Porosity evolution

$V_c = A(H_0 - S)$, where A is the cross-sectional area of the testing chamber, H_0 is the initial packing height of the sample and S is the compactive deformation of the load point. Thus, the stress-dependent porosity is recovered from $\phi = \frac{A(H_0-S)-\frac{m}{\rho}}{A(H_0-S)}$. As shown in Fig. 8b, the porosities in both tests decrease nonlinearly with increasing stress at relatively low stresses. In Test A, the porosity decreases from 0.64 to 0.41 (~ 36%) as stress increases from 0 to ~ 1953 kPa, while for test B, the porosity decreases ~ 23% from 0.66 to 0.51 at the maximum stress of ~ 1592 kPa. Since the applied uniaxial stresses in both tests continuously increase with time, we can compare the porosity changes at the same loading stage. The maximum loading stress of Test A is higher than Test B does and thus the porosity evolutions of the two tests as the applied uniaxial stress increases from 0 to ~ 1592 kPa were compared. The results showed that as applied uniaxial stress increases from 0 to ~ 1592 kPa, the porosity decreases from 0.64 to 0.43(~ 33%) for the uniform stacked material (A) and but only from 0.66 to 0.51 (~ 23%) where the gob is topped with a layer of coarse "roof" rock simulants (B). In addition, the monitored time-dependent loading force and the associated displacements was collected and summarized as a data set, which can be downloaded from the Zenodo website (https://zenodo.org/record/3929410).

Finally, we noted that only materials from the immediate roof were collected and used because the upper caving zone materials are inaccessible. The experimental data plotted here are collected from limited number of tests and thus which may not be inclusive for all the field conditions. The data presented in the work should be cautiously used for further extrapolation. It should be noted that the experimental observations obtained from the two compaction tests on gob materials can provide a justified conceptual model with physical understandings. These experimental results provide at least a preliminary evaluation of the stress–strain behavior for the gob materials. Future studies might incorporate the upper overlying strata, representing the detachment zones, potentially at higher stresses and on larger grades samples.

4 Prediction of Porosity and Permeability Evolution with Compaction

With continuous advancement of the longwall panel, the overlying roof strata behind the support shield may "hang-up" as a rock cantilever before breaking into rock blocks with irregular shapes and sizes within the gob (Fan and Liu 2017).The caved gob will gradually consolidate under the overburden load and porosity and the permeability will evolve with time. Prediction of porosity and permeability is important in defining mitigation strategies to minimize gas (mainly the fugitive methane) concentrations and related hazard. From the compaction experiments in the lab (Fig. 8a), the gob materials show elastic properties as they fully compact, suggesting this as an appropriate model for uniaxial consolidation.

4.1 Stress Distribution within the Caved Gob

In longwall mining, the caved zone can reach 4–11 times the thickness of the mining height where overburden rocks are weak and porous (Karacan 2010). In the caved zone, the broken rock mass stacks layer by layer with continuous caving, as shown in Fig. 9a. Failure begins with the immediate roof strata with the overlying strata sequentially stacking on the gob and loaded by the overburden. Mohr's circle may be used to describe the state of stress in the gob—representing the Mohr–Coulomb failure envelope as shown in Fig. 9b. In Fig. 9b, the vertical stress (the maximum principal stress) can be estimated from the overburden load—average density (kg/m^3) × gravity (m/s^2) × the depth of cover (m). This ignores friction along the boundary between the fragmented rock medium and the rib resulting from movement in vertical direction. As illustrated in Fig. 9b, if the frictional force is ignored, the overburden stress and the horizontal component due to the 'Poisson effect', should be the maximum and minimum principal normal stresses. The Poisson's effect is not accurate to describe the stress variation of horizontal component induced by overburden stress at early compaction stage. The gob is a granulated medium, particularly during early low stress portion when fragments re-orient under load. The horizontal component of in situ stress as the result of tectonic strains seems better approximate the lateral/horizontal stress component. The maximum principal normal stress in the vertical direction increases with an increase in overburden depth with the induced horizontal stress (the minimum principal stress) proportionally increasing (Fig. 9b). For example, as the maximum principal normal stress increases from V_1 to V_2, the corresponding horizontal stress induced by the Poisson effect increases from H_1 to H_2. Theoretically, the overburden stress and the horizontal stress are location dependent, as identified in Fig. 9b, while in practice quantifying them is challenging (this will be discussed in Sect. 6). Simplifying, we assumed that the local overburden stress (σ_v) and the horizontal stress (σ_h) in the following derivations are the average values (Fig. 9a). It should be noted that the shear stress (Fig. 9a) is the combined effects of the horizontal stress and the movement of the rock mass in the vertical direction, based on Amonton's law ($\tau_N = f\sigma_h$, where τ_N is the shear stress and f is the dynamic friction coefficient).

As shown in Fig. 1b, the fragmented rock mass deforms with the overburden load. Due to the Poisson effect, a horizontal stress is applied to the fragmented rock mass by the rib. Due to continuous compaction, the friction force is generated at the rib to resist the vertical displacement of

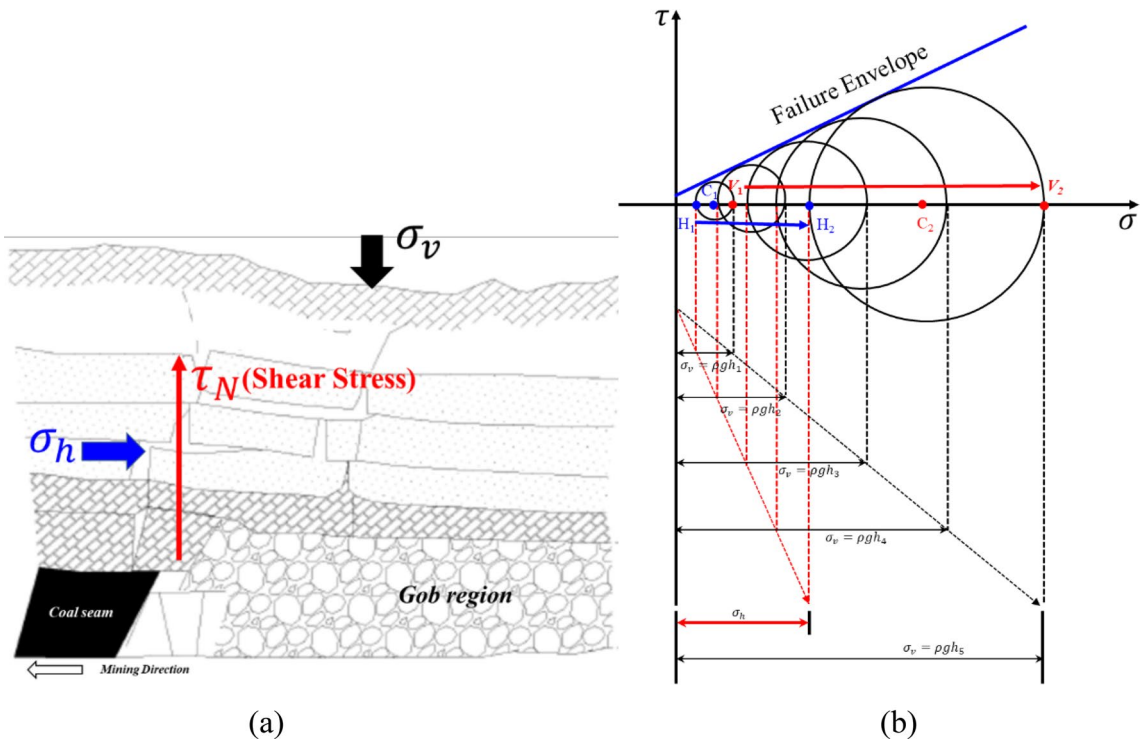

Fig. 9 Schematic of **a** gob compaction and **b** Mohr's circle stress diagram for different cave heights

the compacted rock mass in the loosely compacted Zone B, illustrated in Fig. 1. This induced shear resistance along at the rib changes the state of stress in the loosely compacted Zone B. As illustrated in Fig. 10, the principal stress coordinates at the immediate gob rock mass in Zone B are rotated with the rotation angle depending on the intensity of the shear resistance between the rib and Zone B.

The stress rotation cannot be better described through Mohr's circle in cartesian coordinate system. Rather, Fig. 10a shows the advantages of using a polar coordinate system. For example, if we quantify the normal and shear stresses of plane "A" in the Mohr's circle plot, this represents the plane at an angle β to the maximum principal normal stress direction. In the Mohr's diagram, the deflection angle of this plane is 2β in the Cartesian coordinate system as shown in the Fig. 10. But in the polar coordinate system, the angle between plane "A" and the plane of the maximum principal normal stress is shown directly as the angle β. In the polar coordinate system, the deflection angle of the maximum principal normal stress at the boundary of the loosely compacted Zone B, relative to the vertical direction, is as shown in Fig. 10b. In Fig. 10b, the fragmented rock medium is assumed a porous continuum and the maximum principal normal stress in the center of the caved zone (fully compacted Zone A) is vertical. At the boundary of the caved zone (loosely compacted Zone B), the maximum principal normal stress rotates towards the vertical direction by an angle β. The rib-induced shear resistance requires that the state of the stress for the immediate gob near the rib (Zone B) should be re-analyzed. As quantified in Fig. 10b, the maximum principal normal stress in the center of the caved gob remains vertical with its direction unaffected by the shear stress in the vertical direction (this will be further discussed in Sect. 6). In this study, a representative element volume (REV) is represented by the gob region near the rib (Zone B) and the rotated maximum/minimum principal stresses are regarded as uniform normal stresses applied over the full REV. If the friction force is ignored and the vertical and horizontal stresses are uniformly distributed, the Mohr's circle for the representative element volume (REV) is as shown by the dashed Mohr's diagram (Fig. 11). Here, the Mohr–Coulomb failure criterion is adopted to evaluate the failure state of the rock mass, which can be expressed as

$$\tau = \mu\sigma + C_0, \tag{12}$$

where τ is the shear stress, MPa; σ is the normal stress, MPa; C_0 is the cohesion, MPa; μ is the internal friction coefficient, where $\mu = \tan\varphi$, dimensionless; and φ is the angle of internal friction, degrees.

Since the fragmented rock mass is stacked layer by layer, the rock blocks in the roof fail as the overburden stress increase to its maximum value. We analyze this failure limit—the principal stresses approach this limit as the shear stress reaches the failure envelope. In Fig. 11a, the vertical stress, absent the effect of

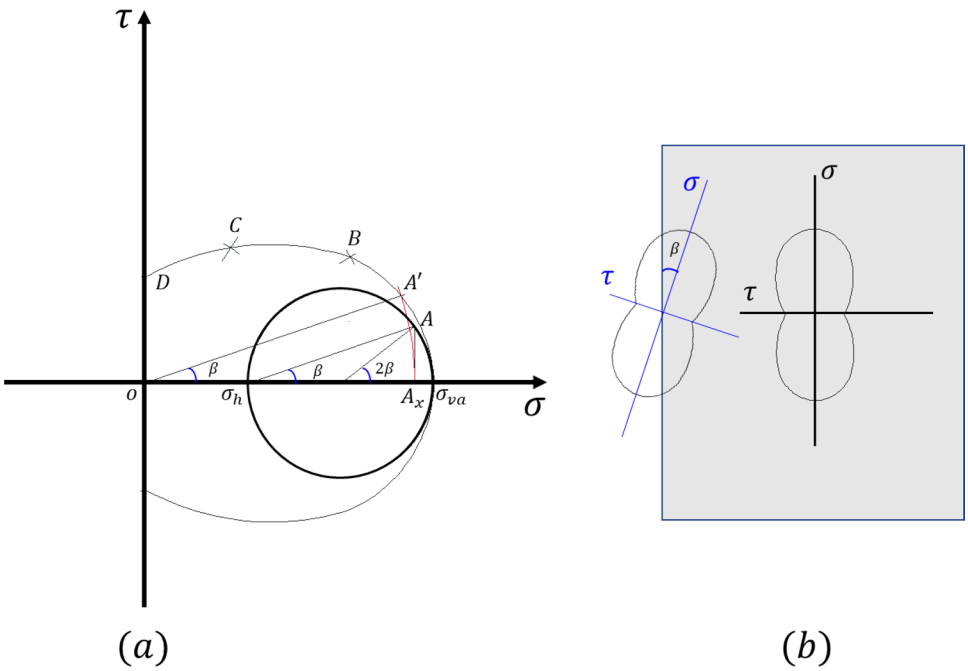

Fig. 10 Mohr's circle stress diagram in **a** Cartesian and polar coordinates, and **b** rotated to the principal coordinates of the system

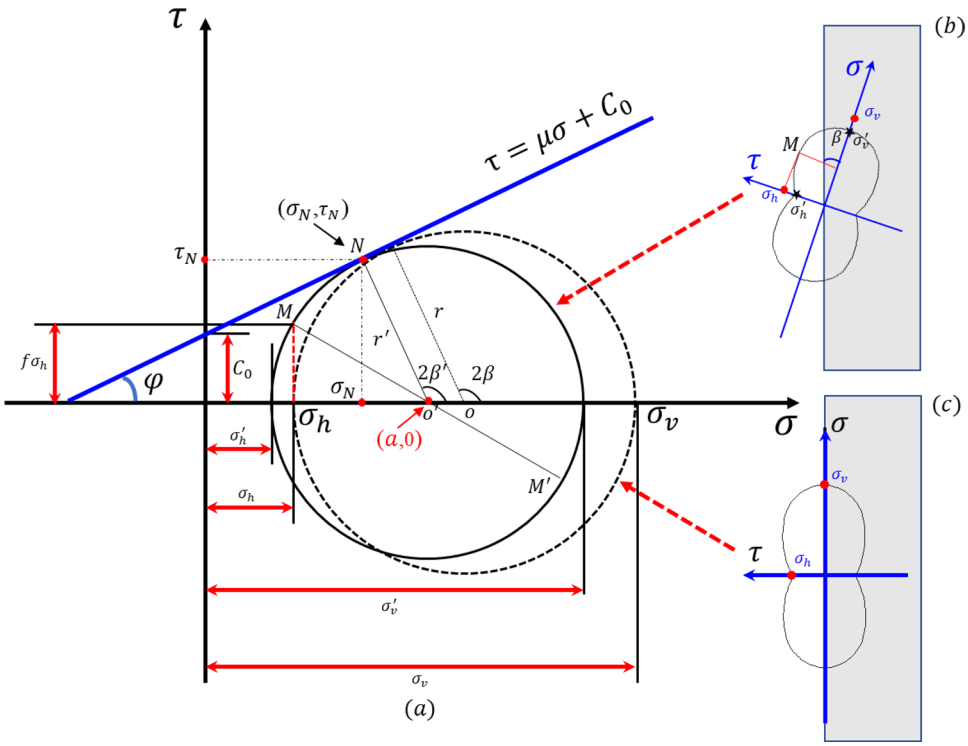

Fig. 11 Rotated Mohr's circle stress diagrams in Cartesian coordinates

friction, is shown as σ_v. This is the maximum principal normal stress with the horizontal stress—that is also the minimum principal stress—is shown as σ_h (Fig. 11c). If the friction force is considered—as shown in Fig. 9a—the plane with the horizontal stress (σ_h) has a shear stress (τ_N) that is perpendicular to the horizontal stress due to the confinement. The rotated Mohr's circle, including the friction force, will pass through location M with coordinates (σ_h,$f\sigma_h$), while the shear stress τ_N can be calculated from $f\sigma_h$ based on Amonton's law (Fig. 11b). The new Mohr's circle will have a revised radius determined by recalling the relationship between the new Mohr's circle and the Mohr–Coulomb failure criterion. Since the fragmented rock blocks are at failure, the radius of the new Mohr's circle may be determined from

$$\begin{cases} \tau_N = \mu\sigma_N + C_0 \\ \dfrac{\tau_N}{\sigma_N - a} = -\dfrac{1}{\mu} \\ (\sigma_h - a)^2 + (f\sigma_h)^2 = (\sigma_N - a)^2 + \tau_N^2 \end{cases} \tag{13}$$

where the location with coordinates (σ_N,τ_N) is the tangent between the new Mohr's circle and the Mohr–Coulomb failure envelope (point N in Fig. 11). Point o' has coordinates (a, 0) and the second equation of Eq. (13) describes the relationship between the tangent (failure envelope) to the Mohr's circle and its radius ($o' - N$).

Based on Eq. (13), the unknown parameter a can be determined as

$$a = \sigma_h + \mu^2\sigma_h + C_0\mu + \sqrt{\mu^2\sigma_h^2 + \mu^4\sigma_h^2 + C_0^2\mu^2 + 2C_0\mu\sigma_h + 2C_0\mu^3\sigma_h - f^2\sigma_h^2 - f^2\mu^2\sigma_h^2 + C_0^2}. \tag{14}$$

Based on the geometry, the radius of the new Mohr's circle (r') can be expressed as

$$\frac{r'}{\sin\varphi} = a + C_0\cot\varphi.. \tag{15}$$

From Eq. (14), the geometric relationship, the maximum principal normal stress in the new Mohr's circle can be expressed as

$$\sigma_v' = (1+\sin\varphi)\left(\sigma_h + \mu^2\sigma_h + C_0\mu + \sqrt{\mu^2\sigma_h^2 + \mu^4\sigma_h^2 + C_0^2\mu^2 + 2C_0\mu\sigma_h + 2C_0\mu^3\sigma_h - f^2\sigma_h^2 - f^2\mu^2\sigma_h^2 + C_0^2}\right) + C_0\cos\varphi. \tag{16}$$

Equation (16) defines the maximum principal normal stress in loosely compacted Zone B by considering the rib resistance. From the new Mohr's circle, the minimum principal normal stress (σ_h') can be calculated as

$$\sigma_h' = (1-\sin\varphi)\left(\sigma_h + \mu^2\sigma_h + C_0\mu + \sqrt{\mu^2\sigma_h^2 + \mu^4\sigma_h^2 + C_0^2\mu^2 + 2C_0\mu\sigma_h + 2C_0\mu^3\sigma_h - f^2\sigma_h^2 - f^2\mu^2\sigma_h^2 + C_0^2}\right) - C_0\cos\varphi. \tag{17}$$

In addition, the plane "M" in the newly formed Mohr's circle defines the redistributed horizontal stress and the associated shear stress along the rib. The horizontal and vertical principal normal stresses must be orthogonal and are therefore defined as in Fig. 10a. The redistributed vertical stress along the boundary can be calculated from point "M'" in the new Mohr's circle (Fig. 11). As a result of shear separation from support provided by the solid ribs, the overburden compaction will be weakened to some extent. As theoretically quantified in Eqs. (16) and (17) and illustrated in Fig. 11, the redistributed principle normal stresses in horizontal and vertical directions will be both lower than their original stress levels with considering shear separation from support provided by the solid ribs.

4.2 Porosity and Permeability Evolution in the Gob

The porosity of the porous medium forming the gob is important in controlling permeability. However, direct measurement of the porosity is difficult, due to its inaccessibility. The porosity of the stacked rock mass will vary with the shapes and size distribution of the fragmented rock blocks. In light of the disordered nature of the fragmented blocks/particles, several successful attempts have been made to characterize soil particle-and aggregate-size distributions by invoking the concept of fractal dimension (Burke and Plummer 1928; Yu and Liu 2004). The fractal dimension links the number size of fragmented particles, as Mandelbrot (1982):

$$N(\omega > \eta) = B_F\eta^{-D_F}, \tag{18}$$

where N is the cumulative number of particles of size ω greater than a characteristic size η, dimensionless; the exponent D_F is the fragmentation fractal dimension; and B_F is a coefficient related to the number of particles of unit diameter, dimensionless.

Fractal theory has also been adopted to characterize the characteristics of the fragmented rock medium in the gob. Typically, the fractal porosity in terms of particle size is given as Karacan (2010)

$$\phi = 1 - \left(\frac{\eta_{min}}{\eta_{max}}\right)^{3-D_F}, \tag{19}$$

where ϕ is the porosity, dimensionless; η_{min} and η_{max} are the minimum and maximum rock block sizes, respectively, m. Based on Eq (19), the initial porosity of the porous medium can be estimated by characterizing the rock sizes and their distribution.

For the fragmented rock mass in the caved gob, the compaction process is uniaxial and thus the associated porosity evolves as a unique function of the variable loading stress in vertical direction. Normally, the porosity of the porous medium can be defined as Kai et al. (2017), Liu and Harpalani (2014a, b), Liu et al. (2020a).

$$\phi = \frac{V_p}{V_b}, \tag{20}$$

where V_p is the void volume, m^3; and V_b is the total volume of the porous medium, m^3.

Based on Eq. (20), the evolution of porosity with uniaxial compaction can be expressed as

$$\begin{aligned}\phi &= \frac{V_b - V_s}{V_b} = 1 - \frac{V_s}{V_{b0}(1-\varepsilon_v)},\\ &= 1 - \frac{V_{s0}}{V_{b0}(1-\varepsilon_v)} = 1 - (1-\phi_0)\frac{1}{(1-\varepsilon_v)},\end{aligned} \tag{21}$$

where V_{b0} is the total volume of the porous medium at an initial time, m^3. Implicit in Eq. (21) is that there is no variation in the solid volume based on an assumed constant rock-medium density. In the caved zone, the initial high void ratio created by the fragmented rocks evolves with time due to the successive compaction of the overburden. With vertical compaction, the broken gob stiffens due to particle rearrangement, slip, and crushing of the fragmented components in the limited caved zone. A reduction in the effective void ratio restricts the fluid pathways to airflow and limits the concurrent migration of methane.

A model quantifying the volumetric strain of the fragmented rock medium is Fan and Liu (2017):

$$\varepsilon_v = \frac{2\lambda + 1}{E_z}\sigma_v, \tag{22}$$

where λ is the confining coefficient representing the intensity of the induced horizontal stress due to overburden compaction, $\lambda = \frac{\sigma_h}{\sigma_v}$, dimensionless; E_z is the uniaxial elastic modulus, MPa. In the rotated principal coordinate system, the confining coefficient (λ) may be expressed as $\lambda' = \frac{\sigma'_h}{\sigma'_v}$, which can be further developed from Eqs. (16) and (17) as

$$\lambda' = \frac{(1-\sin\varphi)\left(\sigma_h + \mu^2\sigma_h + C_0\mu + \sqrt{\mu^2\sigma_h^2 + \mu^4\sigma_h^2 + C_0^2\mu^2 + 2C_0\mu\sigma_h + 2C_0\mu^3\sigma_h - f^2\sigma_h^2 - f^2\mu^2\sigma_h^2 + C_0^2}\right) - C_0\cos\varphi}{(1+\sin\varphi)\left(\sigma_h + \mu^2\sigma_h + C_0\mu + \sqrt{\mu^2\sigma_h^2 + \mu^4\sigma_h^2 + C_0^2\mu^2 + 2C_0\mu\sigma_h + 2C_0\mu^3\sigma_h - f^2\sigma_h^2\left(\frac{x}{b}\right)^2 - f^2\mu^2\sigma_h^2\left(\frac{x}{b}\right)^2 + C_0^2}\right) + C_0\cos\varphi}. \tag{23}$$

In addition, the uniaxial elastic modulus E_z is described as Fan and Liu (2017)

$$E_z = E\left(1 + 2\lambda'\right), \tag{24}$$

where E is the secant modulus, MPa.

By introducing Eqs. (23), (24) into Eq. (22), and then substituting into Eq. (21), the evolving porosity with the increasing vertical stress can be expressed as

$$\phi = 1 - \frac{1-\phi_0}{1 - \frac{(3-\sin\varphi)\left(\sigma_h + \mu^2\sigma_h + C_0\mu + \sqrt{\mu^2\sigma_h^2 + \mu^4\sigma_h^2 + C_0^2\mu^2 + 2C_0\mu\sigma_h + 2C_0\mu^3\sigma_h - f^2\sigma_h^2 - f^2\mu^2\sigma_h^2 + C_0^2}\right) - C_0\cos\varphi}{E(1+2\lambda')}}. \tag{25}$$

The fragmented roof blocks collapse into the caved zone and create viable pathways for airflow and the concurrent migration of methane. The permeability of the zone is related to the size distribution of the fragmented roof blocks—the porosity and the associated permeability are typically used to define the permeability of the gob region. Permeability may be defined through the Carman–Kozeny equation for fluid flow in aggregates that

$$k = \frac{D^2}{180}\frac{\phi^3}{(1-\phi)^2}, \tag{26}$$

where k is the permeability of the packed bed at a specified state, m^2; D is the characteristic size of the aggregate particles, m; and ϕ is the porosity of the porous medium, dimensionless. An equivalent diameter, D, may be defined for a series of particles with irregular shapes—commonly by taking the average of the maximum and minimum particle sizes. However, this may significantly overestimate permeability (Karacan 2010).

Based on Eq. (18), the total number of the particles in the size range η_{min} to η_{max} in the packed bed can be estimated as

$$N_{total}(\omega > \eta_{min}) = B_F\eta_{min}^{-D_F}, \tag{27}$$

where η_{min} and η_{max} are the sizes of the smallest and largest particles, respectively, m. Differentiating Eq. (18) and then dividing by Eq. (27), defines the probability density function of the particle size distribution as

$$\frac{dN}{N_t} = -\frac{D_F\eta^{-D_F-1}}{\eta_{min}^{-D_F}}d\eta. \tag{28}$$

Enabling a characteristic particle size to be defined, based on the probability density function as

$$\tilde{D} = -\int_{\eta_{\min}}^{\eta_{\max}} \frac{-D_F \eta^{-D_F-1}}{\eta_{\min}^{-D_F}} \eta \mathrm{d}\eta = -\frac{D_F \eta_{\max}}{(D_F-1)} \left(\frac{\eta_{\max}}{\eta_{\min}}\right)^{-D_F} + \frac{D_F \eta_{\min}}{(D_F-1)}. \tag{29}$$

By replacing the characteristic size of the aggregate particles and porosity in Eq. (26) by Eqs (29) and Eq. (25) gives

$$k = \frac{\left[-\frac{D_F \eta_{\max}}{(D_F-1)} \left(\frac{\eta_{\max}}{\eta_{\min}}\right)^{-D_F} + \frac{D_F \eta_{\min}}{(D_F-1)}\right]^2}{180} \times \frac{\left[1 - \frac{1-\phi_0}{1-\frac{(3-\sin\varphi)\left(\sigma_h+\mu^2\sigma_h+C_0\mu+\sqrt{\mu^2\sigma_h^2+\mu^4\sigma_h^2+C_0^2\mu^2+2C_0\mu\sigma_h+2C_0\mu^3\sigma_h-f^2\sigma_h^2-f^2\mu^2\sigma_h^2+C_0^2}\right)-C_0\cos\varphi}{E(1+2\lambda')}}\right]^3}{\left[\frac{1-\phi_0}{1-\frac{(3-\sin\varphi)\left(\sigma_h+\mu^2\sigma_h+C_0\mu+\sqrt{\mu^2\sigma_h^2+\mu^4\sigma_h^2+C_0^2\mu^2+2C_0\mu\sigma_h+2C_0\mu^3\sigma_h-f^2\sigma_h^2-f^2\mu^2\sigma_h^2+C_0^2}\right)-C_0\cos\varphi}{E(1+2\lambda')}}\right]^2}. \tag{30}$$

Equation (30) gives the final predictive permeability model of the fragmented rock medium as a result of successive compaction. It is apparent that Eq. (30) can be used to define the permeability evolution of the loosely packed gob region (Fig. 1c) incorporating the effect of stress rotation due to the rib resistance. Also, Eq. (30) can be simplified to describe the permeability evolution in the fully compacted Zone A (Fig. 1c) by neglecting the effects of shear resistance. This model provides an essential link between permeabilities measured at lab scale and application to field scale response. We wanted to point out that the permeability model is a universal model, which is appropriate to describe the central gob and gob abutment. However, it should be noted that the main difference between the central gob and the gob abutment is the stress distribution, which will be discussed in Sect. 6.

5 Results and Analyses

In this study, we first developed the conceptual model based on the physical understandings of the two experiments in Sect. 3. Subsequently, the universal models for quantifying stress, porosity/permeability were proposed in Sect. 4. Since we cannot collect enough experimental data under very high loadings based on our experimental setup (Fig. 4), we tried to use the public data to validate our proposed models. The proposed models are universal models which can be validated via public data. Fortunately, previous scholars provided the well accepted data set, and which really helped us validate the proposed models in this study (Pappas and Mark 1993; Karacan 2010). The public data and the detailed background information were summarized in Appendix 1.

Uniaxial compaction experiments are conducted in this study to augment previous studies (Pappas and Mark 1993). Porosity and permeability evolve with compaction, as quantified in Eqs. (25) and (30). The uniaxial elastic modulus E is a measure of the secant modulus of the fragmented rock medium. Uniaxial compression data are already available for shale, weak sandstone, and strong sandstone (Pappas and Mark 1993). These results show that the secant modulus of the fragmented rock medium is linear with the uniaxial loading stress, which can be expressed as

$$E = (\alpha\sigma_z + b), \tag{31}$$

where a and b are linear fitting parameters.

The secant moduli ($E = \frac{\sigma_z}{\varepsilon_z}$) of the fragmented rock medium are calculated from the nonlinear stress–strain curve of Fig. 12. The nonlinear stress–strain curve shows an initial highly compactive stage, attributed to the high void ratio of the packed zone. With further compaction, the fragment pack stiffens and deformation becomes linear in stress. The fitted values of a and b are then used to calculate the uniaxial elastic modulus based on Eqs. (24) and (31). Figure 12 shows comparisons between the modeled and experimental results for porosity evolution based on Eq. (25). Porosity evolves non-linearly with an increase in stress with good agreement between experimental and modeled data. The modeled porosities show an obvious deviation from the experimental results only at low stresses—due to the assumption of a linear response in stress–strain (Fig. 8a). The fragmented rock blocks in the sample chamber are loosely packed as illustrated in Fig. 7. The loosely packed rock blocks fully compact and transition to elastic response

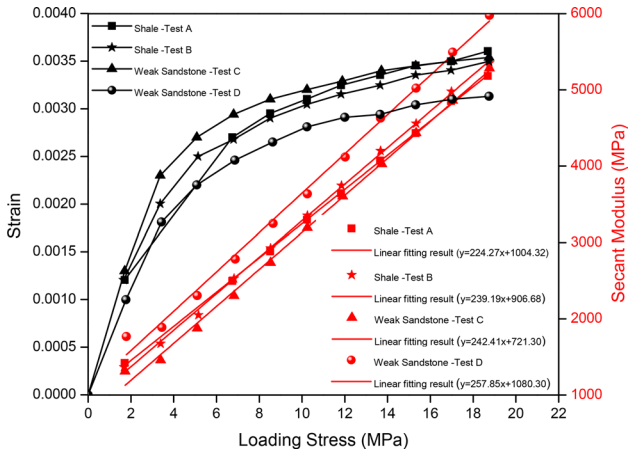

Fig. 12 Stress–strain response and secant modulus for broken rock blocks under successive compaction Data adapted from Pappas and Mark (1993)

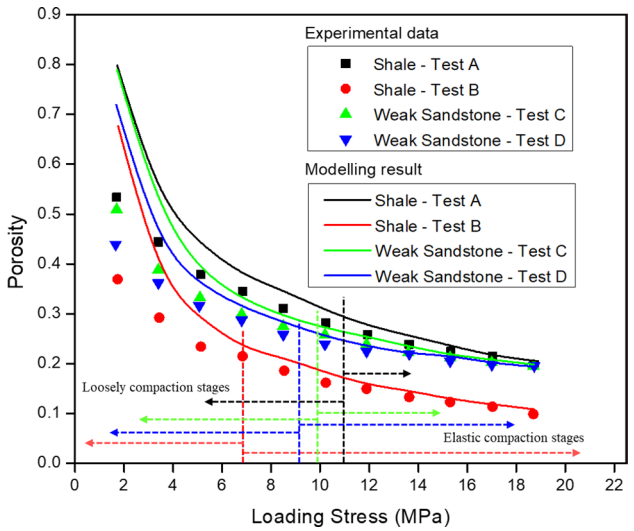

Fig. 13 Comparisons of experimental and modeled porosities Data adapted from Pappas and Mark (1993)

under elevated stresses, as shown in Fig. 13. An approximately 11-fold increase in stress (~ 1.70 MPa to ~ 18.68 MPa) results in a nonlinear decrease in porosity of ~ 63% (from 0.533 to 0.198) for shale Test A, ~ 73% (from 0.369 to 0.099) for shale Test B, ~ 62% (from 0.509 to 0.195) for sandstone Test C, and ~ 56% (from 0.439 to 0.194) for sandstone Test D.

Predictions of permeability evolution have been largely from changes in porosity with magnitudes evolving from 0.026 cm^2 to 0.074 cm^2 for a gob initially composed of larger rocks and from 0.009 to 0.026 cm^2 for smaller rock blocks (Karacan 2010). As proposed in Eq. (26), the permeability of the fragmented rock medium is linked to porosity through the Carman–Kozeny relation. As quantified in the Carman–Kozeny equation, the particle size distribution (characteristic size) of the fragmented rock and the porosity are the only two parameters that determine the associated permeability evolution. Previous studies have estimated the dimension of the broken rock blocks by taking the average of the maximum and minimum dimensions of the aggregates (Karacan 2010). We recover the average dimension directly from the probability density function of the particle size distribution. Figure 14a shows permeabilities of the compacted rock blocks predicted from this model and compares them with previous modeling studies (Karacan 2010). The predicted permeability model is fractal and captures the irregular shapes of the different flow channels including circular, triangular, and elliptical sections. Figure 14a shows the predicted permeabilities of previous studies (Karacan 2010), assuming that flow channels are elliptical in section. The permeability–stress curves divide naturally into two segments—representing the nonlinear initial stage and the linear later (high stress) stage (Fig. 14a). For elliptical flow channels, as the loading stress increases from 0 to 18.68 MPa, the predicted absolute permeabilities for the of shale Test A and the weak sandstone of Test C decrease from 0.0017 to 7.4×10^{-4} cm^2—an 11-fold decrease. Similarly, the predicted permeabilities for the shale of Test B and the weak sandstone of Test D decrease from 0.0037 cm^2 and 0.0017 cm^2, respectively (Karacan 2010). Based on the proposed permeability model, as the loading stress increases from 3.40 to 18.68 MPa, the predicted permeabilities for Tests A, B and D decrease by two orders of two orders of magnitude, from 3.10×10^{-3} cm^2 to 4.18×10^{-5} cm^2 (Test A), from 2.15×10^{-2} to 4.98×10^{-4} cm^2 (B), and from 1.1×10^{-2} cm^2 to 4.58×10^{-4} cm^2 (D), respectively, while for Test C, the permeability decreases from 6.60×10^{-3} to 2.87×10^{-4} cm^2 (C) by one order of magnitude. At low stresses and under loose compaction, the predicted results in our study are distinctly higher than those of previous modeling studies (Karacan 2010). After initial compaction, the newly compacted rock mass behaves elastically and both models predict permeabilities to the same order of magnitude. As illustrated in Fig. 8, the excessive compaction at low stress suggests that initial permeabilities should indeed be high—as implicitly defined for this proposed model in this study. This nonlinear early response is not incorporated in previous permeability models (Karacan 2010), resulting in this mismatch. Prior models mainly consider the size distribution of the broken rock mass, which explains the negligible differences between the predicted permeabilities between the test groups (i.e. Tests A and C, Tests B and D) even though these groups were packed with

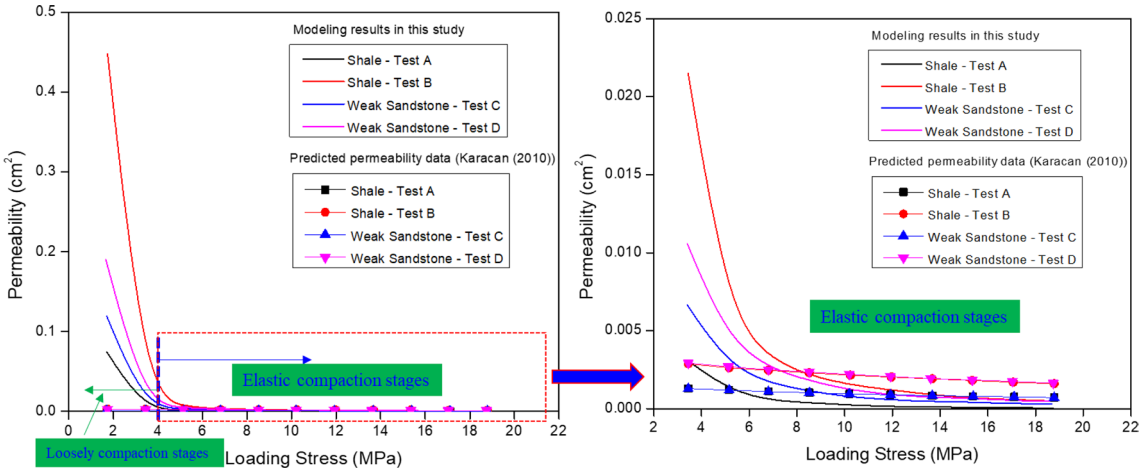

(a)

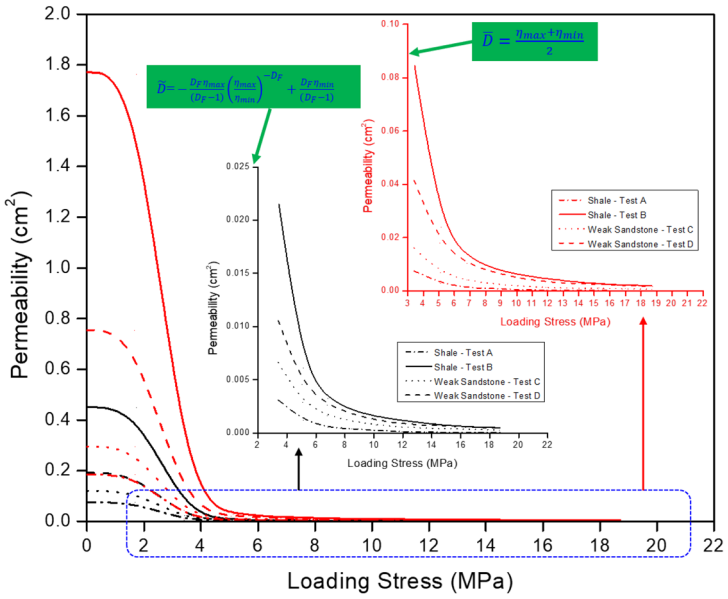

(b)

Fig. 14 Comparisons of experimental observations with modeled permeabilities Raw data adapted from Pappas and Mark (1993)

different types of fragmented rock. Typically, the dimensions of the maximum and minimum particles in Tests A and C are the same but the rock aggregates in Tests A and C exhibit different elastic properties—thus, the apparent volumetric responses exhibit clear differences (Fig. 12). The proposed model in this study accurately predicted the differences of the permeabilities among the test groups for the four rock mass types based on Eq. (30).

The effects of the average dimensions of the particles on permeability predictions are compared in Fig. 14b. The average particle dimensions were taken from the mean value of the maximum and minimum particle sizes ($\bar{D} = \frac{\eta_{\max}+\eta_{\min}}{2}$) as well as estimated from the probability density function (PDF) of the fractal particle size distribution ($\tilde{D}$ in Eq. (29)). As shown in Fig. 14(b), if the average dimensions of the particles are calculated from the maximum and minimum particle sizes, alone, the predicted permeabilities are distinctly higher than those recovered using the PDF. The results illustrate that the form of the size distribution of the particles, and the associated flow architecture, significantly influences the permeability evolution, as confirmed in the experimental observations of Fig. 8.

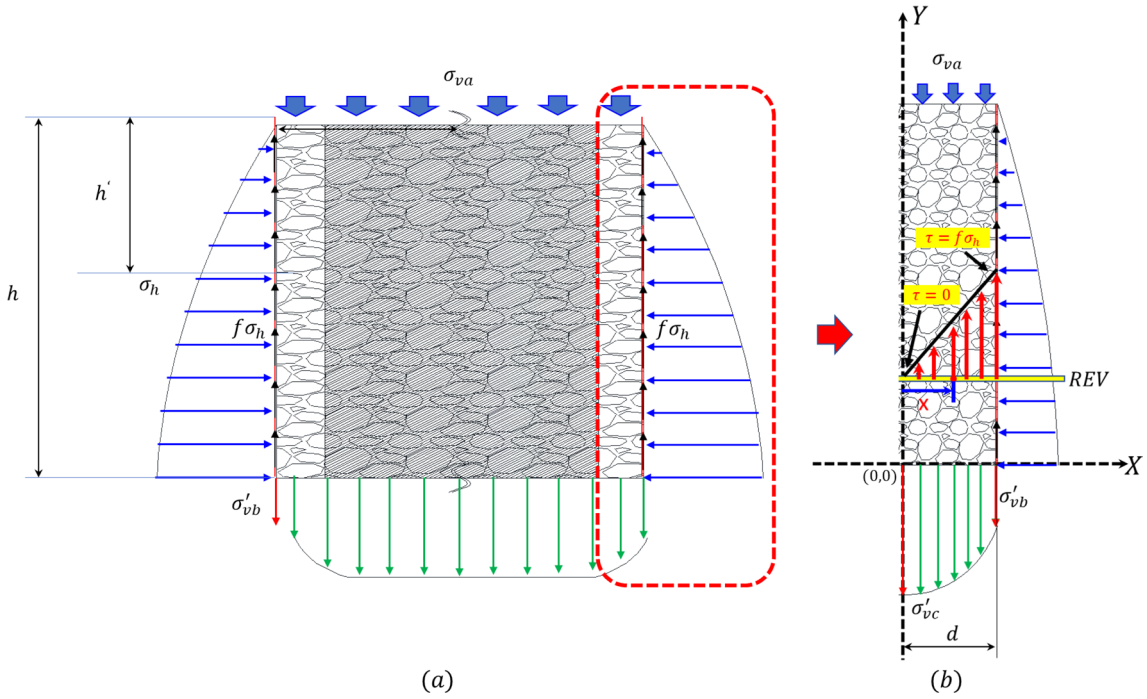

Fig. 15 Schematic of nonuniform distributions of vertical stress in the caved zone

6 Discussion and Improved Understanding of the Gob Compaction

The longwall panel is typically very wide for its productivity, the rib resistance and support effects at the boundary near the rib area will not influence the stress distribution in the middle of the gob region based on the classical Saint-Venant's principle, as illustrated in Fig. 15a. In Fig. 15, the vertical stress in the middle region of the gob flattens out after a certain distance. For our study, we assume the location of gob at three times of the caved zone thickness (h) will reach its maximum based on the Saint-Venant's principle. However, the stress in the loosely compacted area near the fully compacted gob zone will be influenced by the shear stress. The modified vertical stress model demonstrates that the vertical stress in the caved zone varies with locations, as shown in Fig. 15b. Specifically, the average vertical stress in the center of the caved zone is maximum and the minimum vertical stress is expected near the rib area.

In Sect. 4.1, the rotation of the coordinate system representing the principal stresses, as induced by rib resistance, was modeled as shown in Fig. 11. However, it should be noted that the derivations assume that the gob material is subject to uniform stresses—represented as average vertical and horizontal stresses. From the rotated Mohr's circle (Fig. 11a), the modified vertical stress can be calculated from Fig. 11 as

$$\begin{aligned}\sigma_{\mathrm{v}} &= 2\times a-\sigma_{\mathrm{h}},\\ &= 2\Big(\sigma_{\mathrm{h}}+\mu^2\sigma_{\mathrm{h}}+C_0\mu\\ &+\sqrt{\mu^2\sigma_{\mathrm{h}}^2+\mu^4\sigma_{\mathrm{h}}^2+C_0^2\mu^2+2C_0\mu\sigma_{\mathrm{h}}+2C_0\mu^3\sigma_{\mathrm{h}}-f^2\sigma_{\mathrm{h}}^2-f^2\mu^2\sigma_{\mathrm{h}}^2+C_0^2}\Big)-\sigma_{\mathrm{h}}.\end{aligned} \tag{32}$$

Equation (32) defines the vertical stress acting on the loosely compacted gob adjacent to the rib. Thus, the vertical stress in the near-rib region will be less than in the center, as a consequence of rib resistance and support. To capture the nonuniform distribution of the vertical stress in the caved zone (Fig. 15b), we first assume no vertical displacement in the compacted gob at the center line of the

caved zone—illustrated as the Y axis. Due to this symmetry, no shear stress will be induced on the vertical plane of the gob centerline. If there is no shear stress on the centerline, the shear stress at any given vertical plane from the center line to the gob boundary can be defined as

$$\tau = \frac{f\sigma_h}{d}x, \tag{33}$$

where τ is the shear stress on a given vertical plane at a distance x from the centerline ;x is the distance between the centerline and the given plane; and d is the half width of the caved zone.

From Eq. (33), we can define the dynamic friction coefficient at given vertical plane as

$$f' = \frac{\tau}{\sigma_h} = f\frac{x}{d}, \tag{34}$$

where f' is the dynamic friction coefficient on a given plane at a distance x away from the centerline of the gob.

By replacing the boundary friction coefficient f in Eq. (32) as f', the vertical stress at different locations can be expressed as

$$\sigma_v = 2\Big(\sigma_h + \mu^2\sigma_h + C_0\mu + \sqrt{\mu^2\sigma_h^2 + \mu^4\sigma_h^2 + C_0^2\mu^2 + 2C_0\mu\sigma_h + 2C_0\mu^3\sigma_h - f^2\sigma_h^2\left(\frac{x}{d}\right)^2 - f^2\mu^2\sigma_h^2\left(\frac{x}{d}\right)^2 + C_0^2}\Big) - \sigma_h, \tag{35}$$

where Eq. (35) defines the vertical stress at different locations in the caved zone. The modified vertical stress model demonstrates that the vertical stress in the caved zone varies with location, as shown in Fig. 15. From this model for vertical stress, an increase of dynamic friction coefficient results in a corresponding decrease in vertical stress.

7 Summary and Conclusion

In longwall coal mining, the detachment of the undermined roof into the gob leaves a loosely compacted perimeter that skirts the longwall panel. This permeable gob perimeter in plan view forms as a result of shear separation from the rib support. This detachment and the resulting rotated and reduced stresses limit compaction, elevate permeability and exert significant control on gas flow during active longwall mining operations. We report gob compaction experiments using in-mine collected rock fragments stacked in different modes—without (A) and then with (B) a top layer of coarse material. We use a model of the observed compaction behavior to define permeability evolution, in particular, identifying a permeable ring that skirts the compacted gob. Based on this study, the following conclusions can be made:

1 This study documents a load deformation test to observe the volumetric compaction behaviors for the longwall gob material. Experiments were conducted in two modes A and B. As applied uniaxial stress increases from 0 to ~ 1592 kPa, the porosity decreases from 0.64 to 0.43(~ 33%) for the uniform stacked material (A) and but only from 0.66 to 0.51 (~ 23%) where the gob is topped with a layer of coarse "roof" rock simulants (B). Particle–particle self-adjustment dominates the compactive behavior at initial low stress and results in significant strain—followed by a linearly elastic region through the remainder of loading.
2 The granulated gob materials evolve with an initial highly compacting response where particulate readjustment dominates the response, followed by a stiffer response that is near linear between stress and strain. For the continuously coarsening upwards gradation of Test A and Test B, the strains of ~ 0.25 and ~ 0.17 are the thresholds to elastic responses at the average stresses of ~ 0.38 MPa and ~ 0.41 MPa, respectively. The maximum strains for Test A and Test B are ~ 0.39 and ~ 0.30 corresponding to the maximum stresses of ~ 1.95 MPa and ~ 1.59 MPa, respectively, during the second load cycle.

3 The experimental results indirectly demonstrate the "O-shaped" type compaction behavior for the gob materials at lab scale. A loosely compacted gob perimeter develops around the gob as a result of shear collapse and associated shear resistance at the rib support. This zone exhibits a skirting ring of elevated permeability and controls gas flow in and adjacent to the gob and significantly impacts longwall mining operations.

4 The predictive permeability model incorporates the elastic properties of the compacting gob and the size distribution of the component blocks, enabling the known redistribution of stresses to define permeability evolution in the gob. Based on the proposed permeability model, as the loading stress increases from 3.40 to 18.68 MPa, the predicted permeabilities for Tests A, B and D decrease by two orders of two orders of magnitude, from 3.10×10^{-3} to 4.18×10^{-5} cm^2 (Test A), from 2.15×10^{-2} to 4.98×10^{-4} cm^2 (B), and from 1.1×10^{-2} to 4.58×10^{-4} cm^2 (D), respectively, while for Test C, the permeability decreases from 6.60×10^{-3} to 2.87×10^{-4} cm^2 (C) by one order of magnitude.

Acknowledgements This study was sponsored by the Alpha Foundation for the Improvement of Mine Safety and Health, Inc. (ALPHA FOUNDATION). The views, opinions, and recommendations expressed herein are solely those of the authors and do not imply any endorsement by the ALPHA FOUNDATION, its Directors and staff. We also thank our partner mine, Tangkou coal mine, for support and for providing access to the mine for field work. The data used in this study can be downloaded from the Zenodo website (https://zenodo.org/record/3929410).

Compliance with Ethical Standards

Conflict of interest The authors declare no conflict of interest for this manuscript.

Appendix 1

In this study, the raw experiment data for validating the proposed model was cited from Pappas and Mark (1993). In addition, the raw data was also organized by Karacan (2010). Pappas and Mark (1993) conducted compaction tests on gob materials collected from one site in a Virginia mine in the Pocahontas Coalbed, and two sites in an eastern Kentucky mine in the Harlan Coalbed. The test results of each simulated gob material were summarized in Table 2. The particle size distribution before and after corresponding loads were shown in Fig. 16 and the fragmentation fractal dimension D_F was calculated based on Eq. (18) and the results were summarized in Table 3. As shown in Fig. 10, the stress–strain curves were monitored and the corresponding displacements were obtained through the compaction experiments. Based on the stress–strain curves and the initial porosities (Table 2), the stress-dependent porosities can be calculated by referring the methods illustrated in Sect. 3.2.

Table 2 Summary of the four tests from Pappas and Mark (1993) and Karacan (2010)

Test	Rock type	Maximum size (cm)	Maximum stress (MPa)	Initial porosity	Final porosity
A	Shale	5.1	19.0	0.802	0.160
B	Shale	8.9	21.3	0.679	0.078
C	Sandstone	5.1	19.3	0.790	0.152
D	Sandstone	8.9	21.1	0.719	0.162

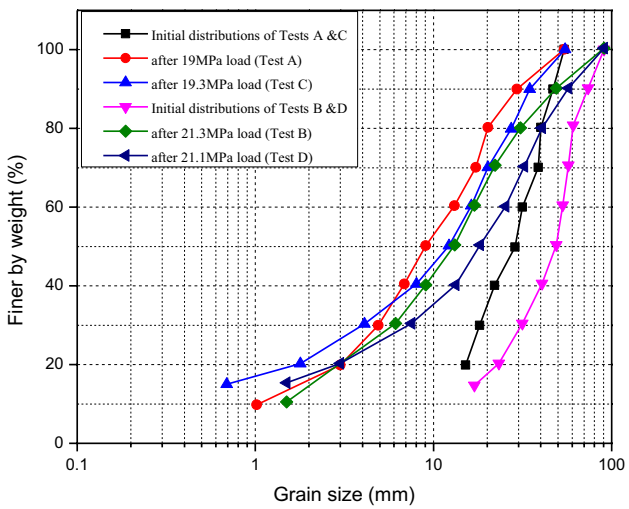

Fig. 16 Particle size distributions of four tests after maximum stress loads (Pappas and Mark 1993; Karacan 2010)

Table 3 Particle size distributions and the associated the fragmentation fractal dimensions of four tests (Pappas and Mark 1993; Karacan 2010)

Test	Before loading		After loading		D_F	
	Minimum size (cm)	Maximum size (cm)	Minimum size (cm)	Maximum size (cm)	Before loading	After loading
A	1.5	5.1	0.5	5.1	2.19	2.89
B	1.7	8.9	0.6	8.9	2.25	2.91
C	1.5	5.1	0.4	5.1	2.19	2.81
D	1.7	8.9	0.8	8.9	2.25	2.87

References

Adhikary DP, Guo H (2014) Modelling of longwall mining-induced strata permeability change. Rock Mech Rock Eng 48:345–359. https://doi.org/10.1007/s00603-014-0551-7

Alehossein H, Poulsen BA (2010) Stress analysis of longwall top coal caving. Int J Rock Mech Min Sci 47:30–41. https://doi.org/10.1016/j.ijrmms.2009.07.004

Arya LM, Paris JF (1981) A physico-empirical model to predict the soil moisture characteristic from particle-size distribution and bulk density data. Soil Sci Soc Am J 45:1218–1227

Auset M, Keller AA (2004) Pore-scale processes that control dispersion of colloids in saturated porous media. Water Resour Res. https://doi.org/10.1029/2003WR002800

Burke SP, Plummer WB (1928) Gas flow through packed columns. Ind Eng Chem 1(20):1196–1200. https://doi.org/10.1021/ie50227a025

Esterhuizen G, Karacan CÖ (2007) A methodology for determining gob permeability distributions and its application to reservoir modeling of coal mine longwalls. SME Ann Meet 88(1):012037

Fan L, Liu S (2017) A conceptual model to characterize and model compaction behavior and permeability evolution of broken rock mass in coal mine gobs. Int J Coal Geol 172:60–70. https://doi.org/10.1016/j.coal.2017.01.017

Forster I, Enever J (1992) Hydrogeological response of overburden strata to underground mining. Off. Energy Rep. 1:104

Guo H, Adhikary DP, Craig MS (2009) Simulation of mine water inflow and gas emission during longwall mining. Rock Mech Rock Eng 42:25–51. https://doi.org/10.1007/s00603-008-0168-9

Guo H, Todhunter C, Qu Q, Qin Z (2015) Longwall horizontal gas drainage through goaf pressure control. Int J Coal Geol 150–151:276–286. https://doi.org/10.1016/j.coal.2015.09.003

Jozefowicz RR (1997) The post-failure stress-permeability behaviour of coal measure rocks. PhD thesis. Univ. Nottingham

Karacan CÖ (2009a) Reconciling longwall gob gas reservoirs and venthole production performances using multiple rate drawdown well test analysis. Int J Coal Geol 80:181–195. https://doi.org/10.1016/j.coal.2009.09.006

Karacan CÖ (2009b) Forecasting gob gas venthole production performances using intelligent computing methods for optimum methane control in longwall coal mines. Int J Coal Geol 79:131–144. https://doi.org/10.1016/j.coal.2009.07.005

Karacan CÖ (2010) Prediction of porosity and permeability of caved zone in longwall gobs. Transp Porous Media 82:413–439. https://doi.org/10.1007/s11242-009-9437-7

Karacan CÖ, Esterhuizen GS, Schatzel SJ, Diamond WP (2007) Reservoir simulation-based modeling for characterizing longwall methane emissions and gob gas venthole production 71:225–245. https://doi.org/10.1016/j.coal.2006.08.003

Li L, Li F, Zhang Y, Yang D, Liu X (2020) Formation mechanism and height calculation of the caved zone and water-conducting fracture zone in solid backfill mining. Int J Coal Sci Technol 7(1):208–215

Liu S, Harpalani S (2014a) Determination of the effective stress law for deformation in coalbed methane reservoirs. Rock Mech Rock Eng 47:1809–1820. https://doi.org/10.1007/s00603-013-0492-6

Liu S, Harpalani S (2014b) Compressibility of sorptive porous media: part 1. Background ana theory. Am Assoc Pet Geol Bull 98:1761–1772. https://doi.org/10.1306/03241413133

Liu A, Liu S, Wang G, Sang G (2020a) Modeling of coal matrix apparent strains for sorbing gases using a transversely isotropic approach. Rock Mech Rock Eng. https://doi.org/10.1007/s00603-020-02159-3

Liu A, Liu S, Wang G, Elsworth D (2020b) Predicting fugitive gas emissions from gob-to-face in longwall coal mines: coupled analytical and numerical modeling. Int J Heat Mass Transf 150:119392. https://doi.org/10.1016/j.ijheatmasstransfer.2020.119392

Lowndes I, Reddish DJ, Ren T, Whittles DN, Hargreaves D (2002) Improved modeling to support the prediction of gas migration and emission from active longwall panels. Mine Vent. https://doi.org/10.1201/9781439833742.ch38

Mandelbrot BB (1982) the fractal geometry of nature. Freeman, New York, pp 23–117

Mortensen NA, Okkels F, Bruus H (2005) Reexamination of Hagen-Poiseuille flow: shape dependence of the hydraulic resistance in microchannels. Phys Rev E Stat Nonlinear Soft Matter Phys. https://doi.org/10.1103/PhysRevE.71.057301

Pappas DM, Mark C (1993). Behavior of simulated longwall gob material. Report of Investigations, US Department of the Interior. Bureau of Miness, RI-9458

Peng S (2008) Coal mine ground control, 3rd edn. Society for Mining, Metallurgy, and Exploration, Englewood

Rieu M, Sposito G (1991) Fractal fragmentation, soil porosity, and soil water properties: I. Theory 55:1231–1238

Sajjad A, Hossein J, Gholamreza Saeedi (2019) Prediction of face advance rate and determination of the operation efficiency in retreat longwall mining panel using rock engineering system. Int J Coal Sci Technol 6(3):419–429

Sirivithayapakorn S, Keller A (2003) Transport of colloids in saturated porous media: a pore-scale observation of the size exclusion effect and colloid acceleration. Water Resour Res. https://doi.org/10.1029/2002WR001583

Wang K, Liu A, Zhou AT (2017) Theoretical analysis of influencing factors on resistance in the process of gas migration in coal seams. Int J Min Sci Technol 27:315–319. https://doi.org/10.1016/j.ijmst.2017.01.011

Wang J, Elsworth D, Wu Y, Liu J, Zhu W, Liu Y (2018) The influence of fracturing fluids on fracturing processes: a comparison between water, oil and SC-CO_2. Rock Mech Rock Eng 51:299–313. https://doi.org/10.1007/s00603-017-1326-8

Wang B, Dang F, Chao W, Miao Y, Li J, Chen F (2019) Surrounding rock deformation and stress evolution in pre-driven longwall

recovery rooms at the end of mining stage. Int J Coal Sci Technol 6(4):536–546

Wang J, Wei W, Zhang J (2020) Theoretical description of drawing body shape in an inclined seam with longwall top coal caving mining. Int J Coal Sci Technol 7(1):182–195

Wu J, Yu B, Yun M (2008) A resistance model for flow through porous media. Transp Porous Media 71:331–343. https://doi.org/10.1007/s11242-007-9129-0

Yu B, Liu W (2004) Fractal analysis of permeabilities for porous media. AIChE J 50:46–57. https://doi.org/10.1002/aic.10004

Zhang C, Zhang L (2019) Permeability characteristics of broken coal and rock under cyclic loading and unloading. Nat Resour Res 28:1055–1069. https://doi.org/10.1007/s11053-018-9436-x

Zhang C, Tu S, Zhang L, Bai Q, Yuan Y, Wang F (2016) A methodology for determining the evolution law of gob permeability and its distributions in longwall coal mines. J Geophys Eng 13:181–193. https://doi.org/10.1088/1742-2132/13/2/181

Zhang C, Tu S, Zhao Y (2019) Compaction characteristics of the caving zone in a longwall goaf: a review. Environ Earth Sci 78:1–20. https://doi.org/10.1007/s12665-018-8037-7

Zhao J, Yin L, Guo W (2018) Stress-seepage coupling of cataclastic rock masses based on digital image technologies. Rock Mech Rock Eng 51:2355–2372. https://doi.org/10.1007/s00603-018-1474-5

Zhao Y, Zhou H, Zhong J, Liu D (2019) Study on the relation between damage and permeability of sandstone at depth under cyclic loading. Int J Coal Sci Technol 6(4):479–492

Zhu W, Li S, Niu L, Liu K, Xu T (2016) Experimental and numerical study on stress relaxation of sandstones disturbed by dynamic loading. Rock Mech Rock Eng 49:3963–3982. https://doi.org/10.1007/s00603-016-1049-2